Lab on a Chip

RSC Publishing

PAPER

View Article Online
View Journal | View Issue

Cite this: *Lab Chip*, 2013, **13**, 2615

High throughput multilayer microfluidic particle separation platform using embedded thermoplastic-based micropumping†

Tohid Fatanat Didar,‡[a] Kebin Li,‡[b] Maryam Tabrizian*[ac] and Teodor Veres*[ab]

We present an integrated thermoplastic elastomer (TPE) based multilayer microfluidic device with an embedded peristaltic micropump and through-holes membrane for high throughput particle sorting and separation. Fluidic and pneumatic layers of the device were fabricated using hot-embossing lithography and commercially available polycarbonate membranes were succcessfully sandwiched between two thermoplastic elastomer fluidic layers integrated to a peristaltic micropumping layer. The integrated peristaltic micropump induces turbulence at the top-microfluidic layer ring which successfully avoids particle aggregation and membrane blocking even at nanorange size. We present herein the general design of the device structure and pumping characteristics for three devices with membrane pore sizes of 10 μm, 5 μm and 800 nm. By using this design we have successfully demonstrated a separation efficiency as high as 99% of polystyrene microbeads with different sizes and most importantly the separation of 390 nm particles from 2 μm beads was achieved. Using this device, we were also able to separate red blood cells with size of about 6–8 μm from osteoblasts typically larger than 10 μm to demonstrate the potential applicability of this platform for biological samples. The produced microfluidic chip operating at flow rates up to 100 μl min^{-1} allows us to achieve efficient high-throughput sorting and separation of target particles/cells.

Received 7th February 2013,
Accepted 27th March 2013

DOI: 10.1039/c3lc50181g

www.rsc.org/loc

1 Introduction

Particle sorting involves excluding desired particles from a suspension based on their properties. Many techniques have been developed for particle sorting which can be categorized into active and passive approaches.[1–3] Active separation employs physical forces from external sources such as dielectrophoretic,[4] optical,[5–7] magnetic,[8–11] or acoustic forces.[12] However, most of them are complicated and expensive due to the need for external fields, and often additional steps which make the device fabrication complex and difficult to integrate with conventional lab-on-chip (LOC) components. On the other hand, passive separation approaches do not utilise external forces but rely on microfluidic behaviour and the interaction of the fluid with the geometries of the microfluidic chip. Passive methods include obstacle induced separation, hydrodynamic filtration,[13,14] pinched flow fractionation,[15] inertia and Dean flow separation.[16,17] Pinches, weirs and posts are common microfluidic obstacle components which are introduced in microfluidic channels to act as filters, preventing particles from entering certain areas. Physical filtering is among the few separation techniques that do not require pre-processing steps or external actuation.

For size-based separation, commercially available membranes can be embedded in microfluidic chips. In addition to being cost effective, they could easily be integrated into a miniaturized instrument. However there are major limitations in using embedded filters for separation applications in microfluidic devices. These limitations can be divided into fabrication issues and operational drawbacks.

From the fabrication point of view, the main limitation is in non-conformal bonding between the commercially available membranes and microfluidic layers (*e.g.* PDMS or glass based devices). In 2008, Luo and Zare[18] reported the fabrication of PDMS based membranes that were easily sandwiched between PDMS substrates, although this required complicated fabrication steps and the minimum pore sizes achieved were around 7 microns. Later, the same group produced smaller pore size membranes, around 3 microns, by aligning two or three membrane layers with a small gap on top of each other.[19] This requires precise control during the aligning step and a small

[a]*Biomedical Engineering Department, McGill University, Montreal, QC H3A 2B4, Canada*
[b]*National Research Council, Life Sciences Division, Boucherville, QC J4B 6Y4, Canada. E-mail: Teodor.Veres@imi.cnrc-nrc.gc.ca; Tel: +1-450-641-5232*
[c]*Faculty of Dentistry, McGill University, Montreal, QC H3A 2B2, Canada. E-mail: Maryam.tabrizian@mcgill.ca; Tel: +514-398-8129*

† Electronic supplementary information (ESI) available. See DOI: 10.1039/c3lc50181g

‡ These authors contributed equally to this article.

misalignment would significantly change the pore size. Conversely, the multiple membrane approach increases the overall depth of the filtering layer, which could cause membrane occlusion during the operation.

For the operation of the device, membrane blocking and low separation flow rates are the main concerns. Laminar flow in microfluidic channels causes particle clogging and membrane blocking. Increasing the shear force of the flow, and/or the pressure difference across the membrane could be implemented to delay the clogging effect or to drive the flow components through the partially clogged perforation. Wei *et al.*[19] proposed the use of a PDMS membrane with pores in defined areas where the membrane acts simultaneously as both a filter and a valve. The dual function of the membrane allows the chip's user to stop irreversible clogging by sequential flushing and filtering. By using this technique, devices with 10 μm pore size membranes were reported for particle/cell separation at flow rates of around 3 μl min^{-1}. Obviously, the operating flow rate is quite low which limits the developed devices' applications for high throughput particle/cell sorting.[20]

Micropumps and microvalves are two important components of microfluidic devices and their integration has been actively pursued over the past few years to entail diverse functionality. Various actuation mechanisms such as piezoelectric, thermo-pneumatic, pneumatic, and electromagnetic have been explored.[21] Among them, peristaltic micropumps driven by injecting compressed air (pressure mode) or a vacuum (vacuum mode) have attracted considerable interest. Most of the pneumatic, membrane-based microvalves and micropumps reported to date are made of PDMS substrates.[22] However, the large scale use of LOC systems requires fabrication technologies and materials amenable for rapid and low-cost fabrication, simple procedures for bonding as well as stable surface treatments for biomolecule capture and immobilization. Hence, it is desirable to develop new technologies for the rapid fabrication of microfluidic devices at low cost, based on thermoplastic elastomers (TPEs) and thermoforming processes, namely hot embossing and injection moulding. TPEs have recently been used as biocompatible substrates for cellular adhesion and guidance,[23] prototyping of miniaturized microfluidic systems for patterning of DNA arrays[24] as well as complex microfluidic devices.[25,26] This was achieved due to TPE's remarkable properties such as soft fabrication, raw material cost and speed of processing which are comparable or superior to PDMS in many aspects. TPE can form water-tight bonding on the thermal plastic substrates similar to polymethylmethacrylate (PMMA) and cyclo-olefin polymers (COP).[27,28] Therefore, in contrast to PDMS substrates requiring oxygen plasma treatment for binding, TPE can be easily bonded with thermoplastic materials to form fully thermoplastic based microfluidic devices.

Herein, we report the fabrication of a fully thermoplastic based multilayer microfluidic device integrating a pneumatic peristaltic micropump and microvalves with embedded commercially available polycarbonate (PC) membrane filters. Pumping characteristics and different pumping modes of the peristaltic micropump are introduced and their separation efficiency is discussed. Separation of microbeads using a 10 μm membrane pore size applying two different pumping modes is demonstrated and each mode's separation efficiency is discussed. Separation of 390 nm particles from 2 μm beads with a separation efficiency of 99% is also presented. To demonstrate the applicability of the device to separate cells of different sizes, separation of red blood cells of 6 to 8 microns from osteoblasts (larger than 10 microns) is also demonstrated.

2 Materials and methods

2.1 Materials

TPE sheets with initial thickness of 300 μm and 1 mm were extruded at a temperature of 165 °C from as-received pellets of Mediprene of 400 M (GLS Corp., McHenry, IL, USA). SU8 photoresist (GM1070 or GM1075) was purchased from Gersteltec, Pully, Switzerland. Photo-plotted transparent films printed at a resolution of 36 000 dpi from NP, Montreal, Canada were used as photo-masks in the fabrication of molds by using standard photolithography processing. The molds used in hot-embossing were treated by vapour phase deposition of trichloro(1*H*,1*H*,2*H*,2*H*-)perfluorooctyl)silane (97%, Sigma-Aldrich Co., St. Louis, MO, USA). The hot-embossing process described later on was performed with an EVG520 system (EV Group, St. Florian am Inn, Schärding, Austria). Isopore polycarbonates (PC) with pore sizes of 10 μm, 5 μm, and 800 nm were purchased from Millipore (Whitby, ON, Canada). Fluorescence micro-/nanobeads were purchased from Thermo-Scientific (Fremont, CA, USA).

2.2 Multilayer microfluidic design

Fig. 1 shows a schematic of the microfluidic design. Fig. 1a is a 3D representation of the design and Fig. 1b depicts a cross-section of the device in the circular channel area. Different layers of the device are also shown in Fig. 1c. The design consists of four layers, *i.e.*, the bottom microfluidic channel layer (BFL), a PC porous membrane layer (ML), the top microfluidic layer (TFL) and a pneumatic air control layer (PL). The bottom fluidic layer (shown in yellow) represents the bottom microfluidic channel with 1 mm width and 100 μm depth. The BFL consists of a circular channel, a straight channel and an outlet. Supporting posts (200 μm in diameter and 100 μm in height with 1 mm spacing) were fabricated in the middle of the bottom fluidic channel to avoid collapse of the membrane layer on the bottom channel. The TFL, coloured in blue, consists of a straight channel for intake of source fluid and outgoing retentate and a circular channel for filtration that is aligned with its corresponding circular ring on the BFL. The TFL has three access holes that can be used as inlets or outlets; depending on the peristaltic micropumping configuration. The PC porous membrane is sandwiched between the bottom and top microfluidic layers. Liquid exchange between the top and bottom microfluidic channels can occur only in the circular channel area. The pneumatic air control layer is

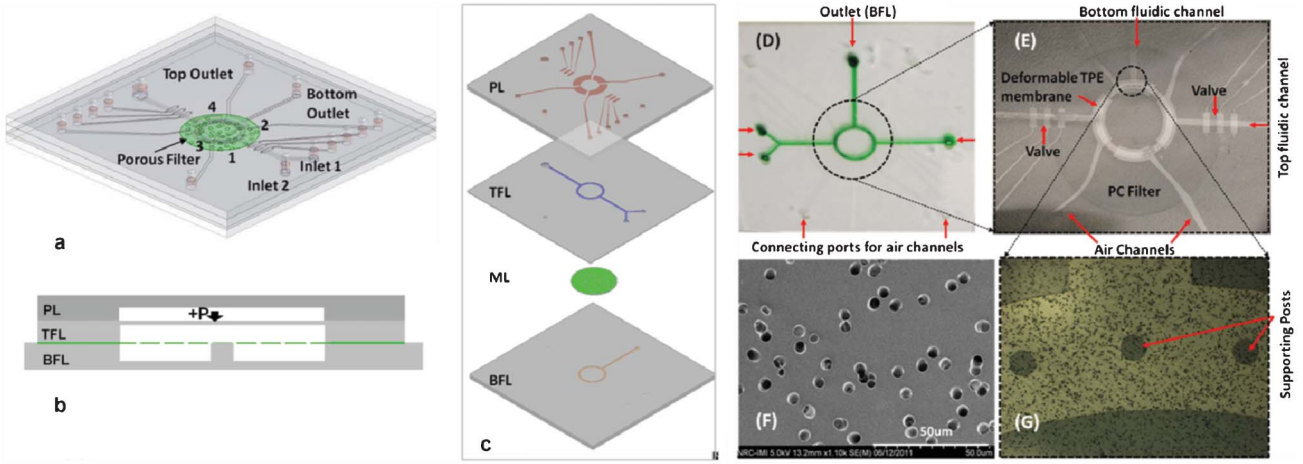

Fig. 1 Multilayer TPE microfluidic design and fabrication. (a) 3D representation of the device, (b) cross-section of the device in the circular channel area, (c) different layers of the microfluidic device, starting from the bottom: bottom fluidic layer (BFL), membrane layer (ML), top fluidic layer (TFL) and pneumatic air layer or pumping layer (PL), (D) a picture of the microfluidic device showing different access holes; both the top and bottom fluidic channels were filled with green colored ink, (E) magnified image of the circular channel area, (F) scanning electron microscope (SEM) image of an embedded polycarbonate membrane with 5 μm pore sizes, (G) optical microscope image of the membrane layer placed on the bottom fluidic layer at the circular channel area intersection with the bottom fluidic channel.

aligned with the top microfluidic layer. The air chamber of the pneumatic air control layer is designed in a fanlike sector which is wider than the channel width of the top microfluidic channel. The top and bottom microfluidic layers, as well as the air control layers, are replicated from a Si wafer patterned with SU8 resist (SU8 molds) by using the hot-embossing technique.

In the introduced design, the peristaltic micropump is operated by the activation of four membranes disposed in a circular fashion. The pumping rate can be increased by increasing the total length of the activation membrane (an increment of the displacement of a single stroke volume) within a relative compact area. This also allows operation of the micropump at high flow rates with higher dynamic back pressure mode, which is very useful in applications requiring higher maximum back pressure.

2.3 Fabrication of the microfluidic device

All of the microfluidic layers (TFL, BFL and PL) were fabricated on TPE by a hot-embossing process on an EVG520 system using SU8 molds. The SU8 molds were produced using standard photolithography techniques. The patterns for the device were printed on transparent films at a resolution of 36 000 dpi which were used as photo-masks. A layer of SU-8 (GM1070 or GM1075) photoresist with a thickness of 100 μm was spin-coated onto a 4 inch silicon wafer, followed by pre-baking at 40 °C for 30 min and at 120 °C for 30 min. It was then exposed to UV light using an EVG 6200 (EV Group, St. Florian am Inn, Schärding, Austria) mask aligner through a transparent mask, followed by a post bake at 95 °C for 1 h. The photoresist development was then performed in propylene glycol monomethyl ether acetate and the wafer was rinsed with isopropanol and dried with a stream of nitrogen gas. It was then hard-baked at 160 °C for 2 h. The SU-8 molds were finally treated with trichloro(1*H*,1*H*,2*H*, and 2*H*-perfluorooctyl)silane using vapour phase deposition to obtain an anti-adhesive layer and to facilitate the release of thermoformed TPE from the mold after hot-embossing.

The maximum operating temperature and embossing force of the EVG520 were 200 °C, and 40 kN, respectively. Heating and cooling modules were active on both upper and lower plates at a rate of 20 and 10 °C min^{-1}, respectively. The base pressure inside the chamber was about 0.1 mbar. Typical embossing conditions were: 5 min at 150 °C with a 10 kN applied force for the bottom microfluidic and pneumatic control layers with a starting thickness of 1 mm. For fabrication of the top microfluidic channel, the starting thickness of the TPE sheets was 0.3 mm. By adjusting the hot-embossing conditions as well as the starting thickness of the TPE sheets, the residue TPE thickness of the top microfluidic channel was controlled between 100 μm and 200 μm in order to avoid collapse of the top microfluidic channel during the operation of the peristaltic micropump and microvalves (up to 15 psi).

Fig. 1D shows a picture of the fabricated microfluidic device. Strong irreversible bonding between the porous filter and TPE layers was achieved and no leakage was observed during the flow testing. Fig. 1F shows a scanning electron microscope (SEM) image of a polycarbonate membrane with 5 μm diameter pore sizes. Fig. 1G depicts an optical microscope image of the bottom microfluidic channel with supporting pillars after placing the PC porous membrane on top of the channel.

Since all the necessary layers were fabricated on TPE, watertight bonding among the TPE layers could easily be formed at room temperature without any additional plasma or thermal treatment. The assembling process of the multilevel microfluidic device was straightforward. Once the BFL was fabricated, the PC porous membrane was placed on top of the TPE layer to cover the circular channel area. Then the TFL, facing down, was aligned on top of the BFL layer under an

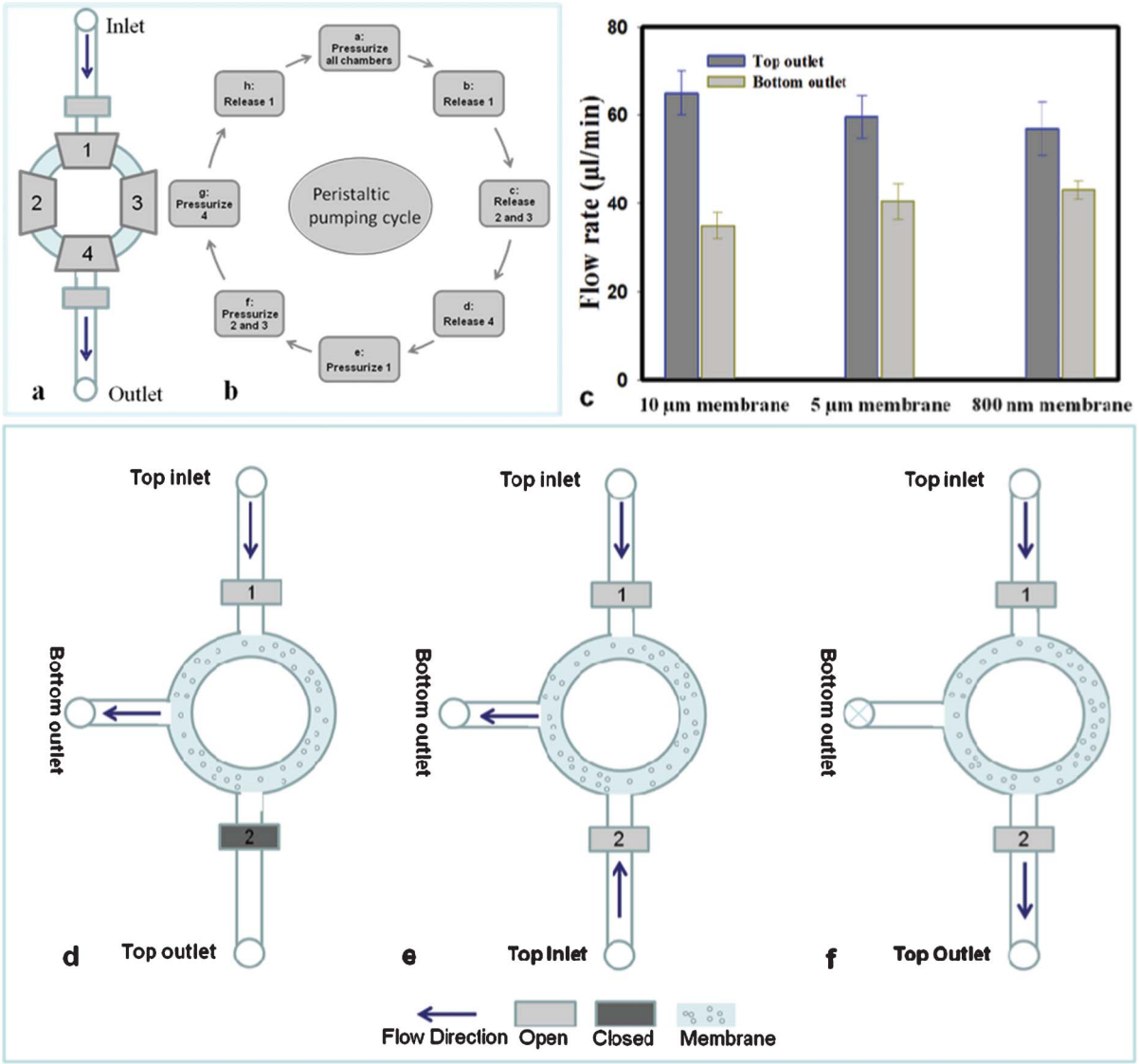

Fig. 2 (a and b) depict a schematic presentation of the circular channel with 4 pneumatic layers for peristaltic micropumping with eight different steps of the peristaltic pumping cycle, (c) measured flow rates for three different chips with 10 µm, 5 µm and 800 nm pore sizes at the top and bottom outlets applying a pressure of 9 psi with a pumping frequency of 3 Hz, (d–f) three different pumping configurations: a top inlet and bottom outlet are used while a top outlet is closed (d), both top access holes are used as inlets and the bottom access hole is an outlet (e) and the bottom outlet is closed and there is flow only in the top microfluidic layer (f).

optical microscope to ensure that the circular channel on the top layer was well aligned with its counterpart on the bottom layer. This was followed by alignment of the PL on top of the TFL using an optical microscope to ensure the air chambers were well aligned with the circular channel of the top microfluidic layer. Finally a hard thermoplastic cover (Zeonor 1060 R) with connecting ports was bonded on top of the assembled device.

2.4 Operation of the embedded peristaltic micropump

Operation of the integrated peristaltic micropump was carried out on a homemade 12-channel pneumatic control manifold. It consisted of 24 electromagnetic valves (EMV) controlled by Lab View Software. The maximum output pressure of the manifold was 30 psi. When the air chamber in the pneumatic control layer is injected with compressed air of a few psi, the residue layer of the TPE is deformed, pushing the liquid underneath forward and backward. A net flow can be generated when more than three membranes are operated in a sequential way and the flow direction is dependent on the membrane activation sequence. This is the typical working principle of a peristaltic micropump based on a three microvalve configuration.[22] As shown in Fig. 2 a and b, a typical peristaltic micropump cycle consists of the following different steps: (1) all four chambers are pressurized, therefore all four TPE membranes are deformed; (2) pressure is released from chamber 1 which is closer to the desired inlet access hole and membrane 1 relaxes back to its initial state aspirating the liquid from the inlet towards the direction of the membrane 1; (3) chamber 1 is kept in the vent state, and the pressure inside

chambers 2 and 3 is simultaneously released, the deformed TPE membranes 2 and 3 relax back to their initial state, resulting in further liquid aspiration from the inlet towards the direction of membrane 1 and then to membranes 2 and 3; (4) chambers 1, 2 and 3 are kept in the vent state and the pressure inside chamber 4 is released, the liquid is therefore aspirated further towards membrane 4; (5) chambers 2, 3, and 4 are in the vent state and chamber 1 is pressurized pushing half of the stroke volume of the liquid back to the inlet direction and the other half towards the outlet direction; (6) chamber 1 is kept in a pressurized state, chambers 2 and 3 are simultaneously pressurized, pushing the liquid towards membrane 4 and then towards the outlet direction; (7) chambers 1, 2 and 3 are kept in the pressure state and chamber 4 is pressurized, pushing the liquid towards the outlet; (8) releasing pressure in chamber 1, restarts aspiration of the liquid from the inlet. Repeating the operation cycle shown in Fig. 2b allows continuous pumping of the liquid from the inlet to the outlet. For the case of the microfluidic design presented herein, the microvalves operated by pneumatic air pressure were integrated on top of the microfluidic channel. Once the sample containing the particles that need to be size separated is introduced in the top circular channel, and the access valve is closed, the sample is then pumped from the inlet to the direction of the circular channel and then passes through the porous filter and eventually the smaller particles are pushed to the bottom outlet. Because of the turbulent agitation of the peristaltic operation mentioned above, the smaller microbeads can efficiently pass through the porous filter to the bottom microfluidic channel and to the bottom outlet. The bigger microbeads remain on top of the filter. To avoid clogging and ensure efficient filtering, after a certain time of circulation on the top circular channel, the liquid containing microbeads larger than the membrane pore size are washed away. The washing liquid that is introduced from inlet 2 is pumped into the circular channel area, and passed through the porous PC filter and then to the bottom outlet to make sure that all the small particles have been pumped to the bottom outlet. Then the valve between the circular channel and the top outlet is opened and therefore the bigger particles are removed from the surface of the PC filter and pumped out from the top outlet. By repeating these two procedures, we can continue the separation of smaller particles without clogging the porous PC filter.

2.5 Sample preparation and analysis

A 15 μm green and 2 μm blue fluorescence microbead suspension was prepared in deionized water with a concentration of 5×10^4 p ml^{-1} each. Mixed suspensions were then prepared with equal volumes of each suspension and used in the experiments. For nanoparticle separation red fluorescence 390 nm particles were prepared at a concentration of 4.5×10^5 p ml^{-1} and mixed with the 2 μm blue fluorescence bead suspension at a concentration of 1.5×10^4 p ml^{-1}.

Initial and collected samples at each outlet were analyzed with an inverted fluorescence microscope (Nikon TE 2000-E). Collected microbeads were further analysed using a fluorescence activated cell sorting (FACS) system. Separated nanosize particles were also assessed using a multi angle particle sizer (Brookhaven Instruments Corporation).

Osteoblasts were cultured in Dulbecco's modified Eagle's medium (DMEM), 10% fetal bovine serum (FBS), and 1% penicillin streptomycin (PS) in a cell culture incubator (at 37 °C, 5% CO_2) and trypsinized prior to all experiments.

3 Results and discussion

3.1 Pumping characteristics of the device

Device operation and flow rates for three different devices using 10 μm, 5 μm and 800 nm membrane pore sizes were investigated. 9 psi pressure with a pumping frequency of 3 Hz was applied and flow rates at the top and bottom outlets were measured simultaneously (Fig. 2c). The overall flow rate at the inlet channel in all three devices was about 100 μl min^{-1}. This flow rate is much higher compared to previously reported microfluidic devices for primary cell purification (3 μl min^{-1} using a 10μm pore size membrane).[20] As depicted in Fig. 2c, the top outlet has a higher flow rate which is expected due to the higher hydrodynamic resistance of the membrane layer. We did not observe significant variation in the top and bottom outlet flow rates using different membrane pore sizes. The slight changes observed ($\pm$3 μl min^{-1}) in the flow rate can be explained by the very small differences in the top and bottom channel width in the circular area due to alignment differences and also because of small changes in the membrane porosity.

3.2 Application to microbead separation

Separation of 2 μm and 15 μm polystyrene microbead populations was performed using a 10 μm pore size membrane by applying two different pumping modes. The separation efficiency, defined as the ratio of the number of target particles to the total number of particles collected at each outlet, was then investigated for both conditions.[19]

In the first configuration, the top outlet valve was closed and the bead mixture entered from the top inlet and passed through the membrane to the bottom outlet (Fig. 2d). This was followed by washing of the membrane using the same pumping configuration to remove any remaining small beads. At the end, the top outlet valve was opened and the 15 μm beads exit from the top outlet (Fig. 2f). 9 psi of compressed air pressure with a pumping frequency of 3 Hz was applied in the pumping layer resulting in a flow rate of about 40 μl min^{-1} from the bottom outlet and 60 μl min^{-1} from the top outlet. Fig. 3l shows collected bead concentrations at each outlet using the aforementioned pumping configuration. Fig. 3a–c show selected images of the initial mixture and collected beads at each outlet channel for the first pumping mode.

For the second pumping configuration, both top fluidic layers' access holes were used as inlets (Fig. 2e). The bead mixture entered from the initial inlet and pure solution containing no beads was introduced from the other top access hole. 9 psi of air pressure with a 3 Hz pumping frequency was used for this purpose and 2 μm beads were collected at the bottom outlet (see ESI† Movie 1). After pumping the mixture, a

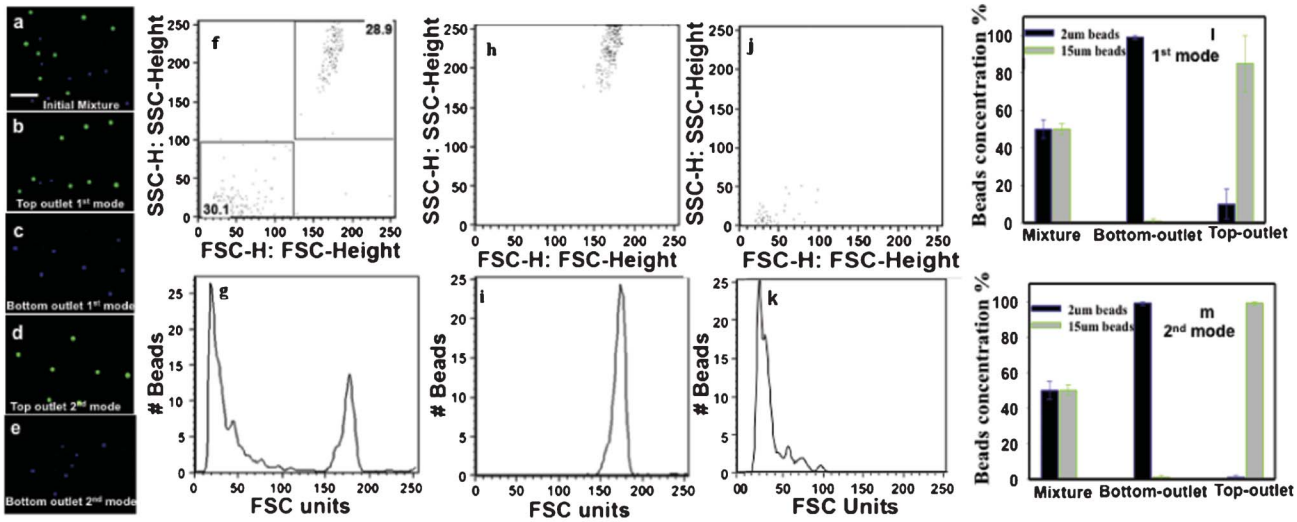

Fig. 3 Microbead separation results. (a–e) selective fluorescence microscopy images of the initial mixture and collected samples at the top and bottom outlets applying two different pumping modes, (f and g) FACS results for size distribution of the initial mixture, (h and i) FACS results for the size distribution of the collected sample at the top outlet on applying the second pumping mode, (j and k) FACS results for the size distribution of the collected sample at the bottom outlet on applying the second pumping mode, (l and m) show mixed bead initial concentrations and collected bead concentrations at the top and bottom outlet channels on applying the first (l) and second (m) pumping modes respectively. Error bars represent standard deviations for the concentration analysis using 10 different fluorescence microscopy images. Scale bar represents 100 μm.

washing step was performed using the same pumping configuration to remove any remaining small beads. Finally, by changing the pumping mode, flow was directed towards the top outlet (Fig. 2f) and 15 μm beads were collected at this outlet. Fig. 3m depicts the collected bead concentrations using this pumping mode. Selected corresponding fluorescence images are also shown in Fig. 3d and 3e. Collected sample analyses using a FACS machine for the second pumping mode are shown in Fig. 3f–g. These results depict the successful separation of beads and confirm the fluorescence microscopy results.

In both pumping modes no 15 μm beads were collected from the bottom outlet. Using the first pumping mode small beads were trapped at the entrance of top outlet channel. Therefore about 15% of the collected sample at the top outlet contained 2 μm beads. This drawback was addressed by changing the pumping mode to the second mode in which the incoming flow from the top outlet channel stopped smaller beads from entering into the top outlet channel. Using the second pumping mode, greater than 99% separation efficiency was achieved for the separation of 2 μm beads from 15 μm beads.

3.3 Application to the separation of sub-micron size particles

The original design of the device allowed the separation of 390 nm from 2 μm beads using a 800 nm membrane pore size and the second pumping strategy (Fig. 2e). After washing the membrane to remove any remaining nanoparticles, 2 μm beads were collected at the top outlet by applying the pumping mode shown in Fig. 2f. Selected fluorescent microscopic images of the initial mixture, bottom outlet and top outlet are shown in Fig. 4a, 4b and 4c respectively. Collected samples from the bottom outlet were analysed using a particle sizer and the results showed a size distribution of 392 nm with a standard deviation of 5 nm. These results indicated an efficiency of higher than 99% for the separation of 390 nm particles from 2 μm beads (Fig. 4d).

3.4 Turbulent washing efficiency and membrane blocking

As mentioned, particle aggregation and membrane clogging are the main operational limitations for membrane based microfluidic separation devices as a result of laminar flow in microfluidic chips. To overcome these limitations, a peristaltic micropump was embedded inside the chip to create necessary turbulence to avoid blocking of the membrane, but also provide the ability to rapidly change the flow direction for optimum separation. Fluorescent images in Fig. 4e–h show the membrane surface area in the circular channel at different steps of the separation process for the separation of 2 μm–15 μm and 2 μm–390 nm particles. Fig. 4e depicts the presence of 15 μm beads on the membrane surface after the pumping step using the 10 μm pore size chip. The same surface is shown in Fig. 4f after the washing step where only a few beads could be found on the membrane surface. Fig. 4g and 4h are fluorescent images of the 800 nm membrane surface in the circular channel after collecting 390 nm particles and the washing step, respectively. Almost all of the 2 μm beads attached to the membrane surface in this area could be detached and collected. These results indicate that the turbulence enabled the removal of undesired particles from the surface allowing repeated use of the chip without further cleaning of the membrane area.

3.5 Biological application of the multilayer microfluidic device

To demonstrate that the device can potentially be used for the separation of biological microparticles such as cells, red blood

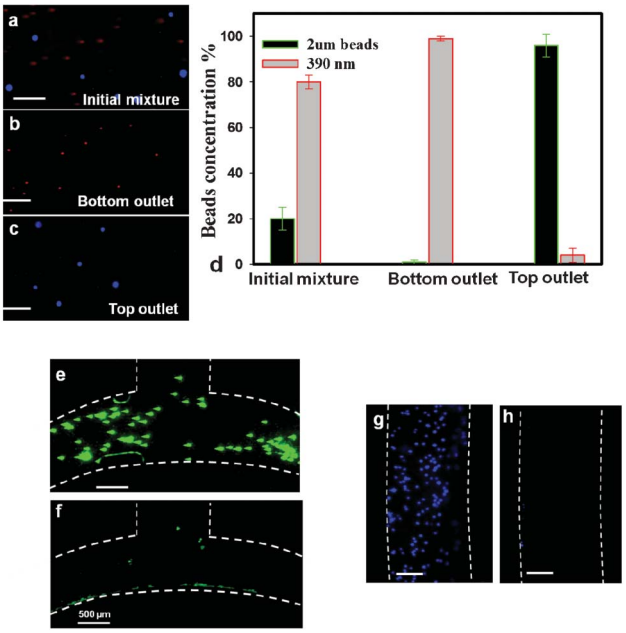

Fig. 4 Results for the separation of 390 nm particles and 2 µm beads. (a, b and c) are selected fluorescence microscopy images of the initial mixture and collected samples at each outlet. Scale bars represent 50 µm. (d) depicts the concentration of each particle in the initial mixture and the collected samples from the bottom and top outlets. Error bars represent standard deviations for the concentration analysis using 10 different fluorescence microscopy images. (e and f) represent the 10 µm pore size membrane surface after pumping and washing steps, respectively (used for separation of 2 µm beads from 15 µm beads). Both images show the same area of the circular channel. (g and h) show the 800 nm pore size membrane surface after the pumping and washing steps, respectively (used for separation of 390 nm beads from 2 µm beads). Both images show the same area of the circular channel. All together, these images indicate that bigger particles can be successfully removed and collected from the membrane surface without any aggregation or blocking. Scale bars in (g) and (h) represent 400 µm.

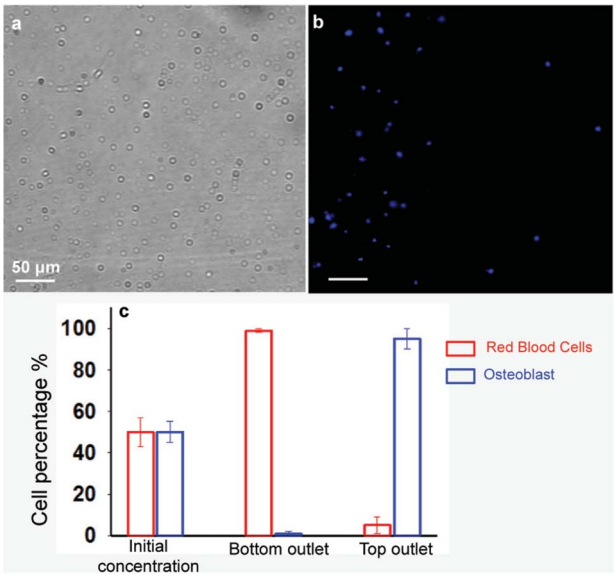

Fig. 5 (a) Optical microscope image of collected red blood cells from the bottom outlet. (b) Collected osteoblasts from the top outlet live stained with Cy5 conjugated dye. No osteoblast cells were collected at the bottom outlet. Scale bars represent 50 µm. (c) Quantitative analysis of the initial cell mixture and collected cells from the bottom and top outlets.

cells (6 to 8 microns) and osteoblasts (larger than 10 microns) were mixed at a concentration of 10^5 cells ml^{-1} each. Osteoblasts were live stained with a fluorescent dye prior to mixing. The second pumping mode (Fig. 2e) with a 10 µm pore size membrane was implemented to separate and collect red blood cells from the bottom and osteoblasts from the top outlets. Analysis of the collected samples showed that more than 99% of the cells collected at the bottom outlet were red blood cells and that the top outlet contained greater than 95% osteoblast cell types (Fig. 5).

4 Conclusion

A microfluidic microparticle separation platform with an embedded peristaltic micropumping system and commercially available membranes was presented for particle/cell separation. The introduced multilayer microfluidic platform was fabricated using hot-embossing lithography on thermoplastic elastomeric substrates providing high-throughput fabrication and lower cost compared to PDMS based devices. Because of the intrinsic mechanism of the peristaltic micropump, the generated turbulent recirculation of particles above the membrane resulted in high separation efficiency without membrane clogging. More than 99% separation efficiency was achieved for both micro- and nanosize particle separation using different membrane pore sizes. As a proof of concept for biological applications, the separation of red blood cells from osteoblasts was demonstrated. The operating flow rate of up to 100 µl min^{-1} provides high-throughput sorting and separation of particles which is a significant advantage compared to previously reported microchips. We showed that the developed platform can be used to integrate commercially available membranes with desired pore sizes to separate a wide range of particle sizes, eliminating the limitations of PDMS membranes to achieve smaller pore sizes. Combined with the desired characteristics of the TPE materials and the multilayer structure of the device, the introduced platform can be easily modified for multi-level particle/cell separation with different size ranges.

Acknowledgements

The authors would like to acknowledge the National Research Council of Canada, National Science and Engineering Research, Council of Canada-Collaborative Research program and Discovery program, Genome Canada/Génome Québec, for their financial support for the development of microfluidic platforms and diagnostic tools. We would like to thank Dr. Christina Holmes for her help regarding FACS. T. F. D. would like to thank the Faculty of Medicine at McGill and Fonds de Recherche du Quebec-Nature et Technologies (FQRNT) for financial support.

References

1 T. F. Didar and M. Tabrizian, *Lab Chip*, 2010, **10**, 3043–3053.
2 A. Lenshof and T. Laurell, *Chem. Soc. Rev.*, 2010, **39**, 1203–1217.
3 K. Sun Min, L. Sung Hoon and S. Kahp Yang, *Lab Chip*, 2008, **8**, 1015–1023.
4 I. Barbulovic-Nad, X. Xuan, J. S. H. Lee and D. Li, *Lab Chip*, 2006, **6**, 274–279.
5 C.-C. Lin, A. Chen and C.-H. Lin, *Biomed. Microdevices*, 2008, **10**, 55–63.
6 A. Jonas and P. Zemanek, *Electrophoresis*, 2008, **29**, 4813–4851.
7 M. M. Wang, E. Tu, D. E. Raymond, J. M. Yang, H. Zhang, N. Hagen, B. Dees, E. M. Mercer, A. H. Forster, I. Kariv, P. J. Marchand and W. F. Butler, *Nat. Biotechnol.*, 2005, **23**, 83–87.
8 E. K. Dirican, O. D. Ozgun, S. Akarsu, K. O. Akin, O. Ercan, M. Ugurlu, C. Camsari, O. Kanyilmaz, A. Kaya and A. Unsal, *J. Assisted Reprod. Genet.*, 2008, **25**, 375–381.
9 K. Hoshino, Y.-Y. Huang, N. Lane, M. Huebschman, J. W. Uhr, E. P. Frenkel and X. Zhang, *Lab Chip*, 2011, **11**, 3449–3457.
10 Y. Zhou, Y. Wang and Q. Lin, *J. Microelectromech. Syst.*, 2010, **19**, 743–751.
11 D. Issadore, H. Shao, J. Chung, A. Newton, M. Pittet, R. Weissleder and H. Lee, *Lab Chip*, 2011, **11**, 147–151.
12 A. Nilsson, F. Petersson, H. Jonsson and T. Laurell, *Lab Chip*, 2004, **4**, 131–135.
13 L. R. Huang, E. C. Cox, R. H. Austin and J. C. Sturm, *Science*, 2004, **304**, 987–990.
14 J. Takagi, M. Yamada, M. Yasuda and M. Seki, *Lab Chip*, 2005, **5**, 778–784.
15 A. A. S. Bhagat, H. W. Hou, L. D. Li, C. T. Lim and J. Han, *Lab Chip*, 2011, **11**, 1870–1878.
16 J. Zhu, T. R. J. Tzeng and X. Xuan, *Electrophoresis*, 2010, **31**, 1382–1388.
17 S. S. Kuntaegovvdanahalli, A. A. S. Bhagat, G. Kumar and I. Papautsky, *Lab Chip*, 2009, **9**, 2973–2980.
18 Y. Luo and R. N. Zare, *Lab Chip*, 2008, **8**, 1688–1694.
19 H. Wei, B.-h. Chueh, H. Wu, E. W. Hall, C.-w. Li, R. Schirhagl, J.-M. Lin and R. N. Zare, *Lab Chip*, 2011, **11**, 238–245.
20 R. Schirhagl, I. Fuereder, E. W. Hall, B. C. Medeiros and R. N. Zare, *Lab Chip*, 2011, **11**, 3130–3135.
21 C. Zhang, D. Xing and Y. Li, *Biotechnol. Adv.*, 2007, **25**, 483–514.
22 M. A. Unger, H. P. Chou, T. Thorsen, A. Scherer and S. R. Quake, *Science*, 2000, **288**, 113.
23 M. D. Guillemette, E. Roy, F. A. Auger and T. Veres, *Acta Biomater.*, 2011, **7**, 2492–2498.
24 M. Geissler, E. Roy, G. A. Diaz-Quijada, J. C. Galas and T. Veres, *ACS Appl. Mater. Interfaces*, 2009, **1**(7), 1387–1395.
25 E. Roy, M. Geissler, J. C. Galas and T. Veres, *Microfluid. Nanofluid.*, 2011, **11**, 235–244.
26 E. Roy, J. C. Galas and T. Veres, *Lab Chip*, 2011, **11**, 3193–3196.
27 E. Roy and T. Veres, Microfluidic Device, Compositions and Method of Forming, *US Patent Application* 12/588, 236, 2009.
28 E. Roy, J. C. Galas and T. Veres, Semipermanently Closed Microfluidic Valve, *International Appl.*, no.: PCT/CA2010/000636, 2010.

